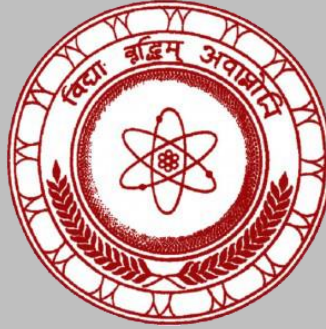


ISSN 1391-0256

Journal of the Sri Lanka Association for the Advancement of Science

Volume 2 Issue 2 2019



Founded in 1944 and incorporated by the Act of Parliament No 11 of 1966.

JSLAAS

Journal of the Sri Lanka Association for the Advancement of Science is a biannual publication. Selected research work from annual research sessions (based on scientific merit) as well as other research articles are invited to submit research manuscripts as per the guidelines provided by SLAAS. SLAAS members may also separately submit their papers for publication. The Journal can be accessed on-line to view and download the full text of the articles published respective to the volumes free of charge

Submission Manuscript

Printed copies of the manuscript in triplicate along with a soft copy could be sent to the Secretary, Sri Lanka Association for the Advancement of Science, "Vidya Mandiraya" 120/10, Wijerama Mawatha Colombo 07, Sri Lanka.

E.mail: hqslaas@gmail.com

Web: www.slaas.lk

Members of the Editorial Board

Editor in Chief

Dr. R. D. Gunaratne
SLINTEC Academy
Sri Lanka Institute of Nanotechnology
Pitipana, Thalagala Rd, Homagama, Sri Lanka.
email: ranildg@yahoo.com

Executive Editors

Dr. R. Chinthaka L. De Silva
Material Technology Section
Industrial Technology Institute,
363, Bauddhaloka Mw, Colombo, Sri Lanka.
email: chinthakades@yahoo.com

Prof. Chandana Jayaratne
Department of Physics
University of Colombo,
Sri Lanka.
email: chandana Jayaratne@gmail.com

Prof. Preethi Udagama
(General President SLAAS 2019)
Senior Professor
Department of Zoology and Environment Sciences
University of Colombo
Sri Lanka
email: preethi @zoology.cmb.ac.lk

Sectional Editors

Dr. M N Kaumal
Dr. Chandana Jayawardena
Prof Lalini Rajapaksha
Prof. Thakshila Serasinghe
Prof. K K Y W Perera

Prof. Manjula Vithanapathirana
Prof. Jayantha Wijeyaratne
Prof. Dhammika Thantrigoda
Prof. Tuley De Silva
Prof. Asoka Karunanada

Exchanges: Please address all requests to the Secretary, *Sri Lanka Association for the Advancement of Science, "Vidya Mandiraya" 120/10, Wijerama Mawatha Colombo 07, Sri Lanka*

ISSN 1391-0256 Copyright © 2019 by the Sri Lanka Association for the Advancement of Science, Sri Lanka. All rights reserved

Table of Contents

	Page
1. The impact of endoplasmic reticulum calcium concentration on transient cytosolic calcium response in phospholipase-C pathway: A simulation study J. T. H. Lakmal and S. P. Rajapaksha	4
2. Mathematical Modelling of Step Shape Bed Forms Generated by Turbidity Currents without incorporating the Wave Entrainment Impact H.M.K.N.Herath,* S.D.Sirithunge and D.D.Dias	14
3. Sodium nickel phosphate cathodes used for sodium-ion rechargeable batteries	27

The impact of endoplasmic reticulum calcium concentration on transient cytosolic calcium response in phospholipase-C pathway: A simulation study

J. T. H. Lakmal and S. P. Rajapaksha

Department of Chemistry
University of Sri Jayewardenepura, Nugegoda, Sri Lanka.

ABSTRACT

Plasma membrane G-protein coupled receptors selectively bind with a diverse array of ligands/drugs to evoke many downstream biological reaction pathways. One of such main pathways is the phospholipase-C (PLC) pathway, which hydrolyses phosphatidylinositol 4,5-bisphosphate (PIP₂) to inositol trisphosphate (IP₃) and diacylglycerol. IP₃ activates IP₃ receptors (IP₃R) in the endoplasmic reticulum (ER) membrane, initiating a burst release of Ca²⁺ from ER to cytosol. The release of Ca²⁺ from ER in the PLC pathway transiently increases [Ca²⁺]_C by several fold. [Ca²⁺]_{ER} is reported to be around 350-400 μM, though this concentration is subjected to fluctuation in certain circumstances. In this research we investigated the effect of [Ca²⁺]_{ER} on the cytoplasmic transient calcium increase during the PLC pathway. Virtual-cell (VCELL), a software platform for modelling and simulation of living organisms/cells, and previously reported initial concentrations and reaction rates were used in the modelling. [Ca²⁺]_C regulators namely smooth endoplasmic reticulum Ca ATPases, plasma membrane Ca ATPases, ryanodine receptors, leak channels and IP₃R were modelled. IP₃ was directly added to the cytosol. According to our results, the increase of the [Ca²⁺]_C and time to peak response from the addition of IP₃ in PLC pathway depend on the [Ca²⁺]_{ER}. Therefore, we suggest that any study to investigate the cytosolic calcium signaling is necessary to study and report the [Ca²⁺]_{ER} to correctly interpret the experimental observations.

Key words: G-protein coupled receptors, phospholipase-C pathway, calcium dynamics, inositol trisphosphate, virtual-cell

INTRODUCTION

Calcium ions are an important cellular secondary messenger, which evokes many downstream reactions including exocytosis, gene transcription, cell proliferation, and muscle contraction (Kanayo Satoh, 2011). However, cells strictly maintain their intracellular concentration of calcium at around 100 nM. Many intra- and extracellular processes involve regulating cellular calcium, which is crucial to make calcium an important second messenger (Rosario Rizzuto, 2009). The tight control mechanism of calcium can be disturbed by two courses: Ca²⁺ ions coming from the extracellular milieu, and the release of Ca²⁺ ions from the calcium stores in the cells (endoplasmic reticular and mitochondrial) (Rosario Rizzuto, 2009). A transient release of calcium from intracellular calcium stores upon receiving an external stimulus initiates many downstream calcium depended pathways before the cell recovers back to its regular calcium condition. There are several ways to induce calcium release from intracellular stores. G-protein coupled receptors (GPCR) represent a major calcium releasing membrane protein category. GPCRs are critical eukaryotic signal transduction proteins, which share a common structure of seven transmembrane helices (Raymond C. Stevens, 2014). GPCRs have an extracellular N-terminus and cytoplasmic C-terminus (Yamauchi T, 2003). GPCRs that couple to G_q proteins can mobilize intracellular Ca²⁺ via activation of phospholipase C (PLC)

pathway(Lisa A. Selbie, 1998). Various types of extracellular stimuli can bind with G_qPCRs to initiate a signal: Acetylcholine, **Oxotremorine-M**, etc. A summarized picture of the PLC pathway is shown in **Figure 1**.

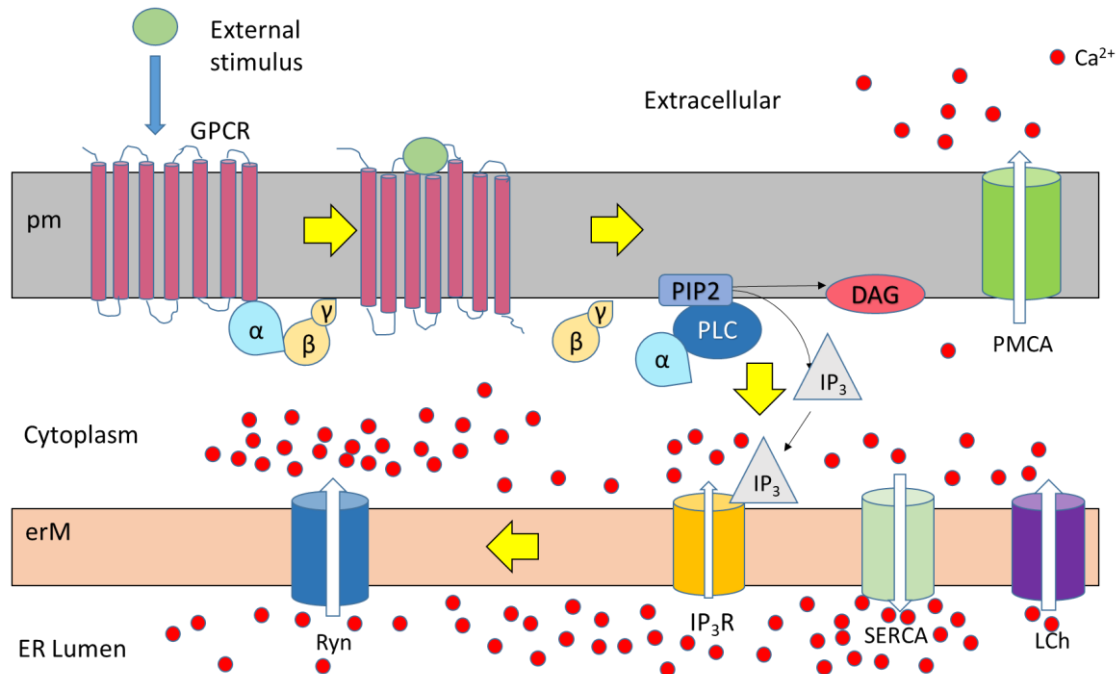


Figure 1: Summarized PLC pathway. pm: Plasma membrane; erM: ER membrane; GPCR: G-protein couple receptor; PLC: Phospholipase C enzyme (PLC); PIP₂:phosphatidylinositol-4,5-bisphosphate; IP₃: Inositol-1,4,5-triphosphate; DAG: diacylglycerol; IP₃R: Inositol-1,4,5-triphosphate receptors; Ryn: Ryanodine receptors; PMCA: Plasma membrane calcium ATPases; SERCA: smooth ER calcium ATPases; LCh: Leak channels. Yellow arrows point the direction of the pathway.

G-proteins consist of three sub units: α , β , and γ . The β and γ subunits are tightly attached to each other, and with the binding of external stimulus, the heterotrimeric G-protein complex dissociates to α subunit and $\beta\gamma$ subunit(Lisa A. Selbie, 1998). The dissociated $\beta\gamma$ subunit remains on the cell membrane, while the alpha subunit leaves the membrane to bind Phospholipase C enzyme, activating it. This enzyme hydrolyses the membrane phospholipid, phosphatidylinositol-4,5-bisphosphate (PIP₂) forming diacylglycerol (DAG) and inositol-1,4,5-triphosphate (IP₃). DAG remains attached to the inner leaflet of the cell membrane, while the IP₃ formed is released into the cytoplasm. IP₃ binds with Inositol-1,4,5-triphosphate receptors (IP₃R) on the ER membrane(Wojcikiewicz, 2012). When IP₃ binds with IP₃R, it causes a sudden release of calcium ions to the cytoplasm from the ER, triggering many other pathways, initially to increase and then to decrease calcium in the cytoplasm (Michael J. Berridge, 2003). Ryanodine receptors (Ryn) in the ER membrane sense the local increase of calcium by IP₃R and trigger a burst release of calcium from ER, resulting in a global calcium increase in the cell. Plasma membrane calcium ATPases (PMCA) and smooth ER calcium ATPases (SERCA) in cell membrane and ER membrane, respectively, remove excess calcium from the cytoplasm. Leak channels (LCh) in the ER membrane work according to the

concentration gradient of calcium between the ER and the cytoplasm. Calcium buffering proteins and calcium sensitive dyes or proteins in the cytosol are also involved in removing transiently increased excess calcium during PLC pathway. The release of Ca^{2+} from the ER in the PLC pathway transiently increases cytoplasmic Ca^{2+} concentration ($[\text{Ca}^{2+}]_c$) by several fold, decreasing the calcium in ER ($[\text{Ca}^{2+}]_{\text{ER}}$). Calcium release from the endoplasmic reticulum is inhibited progressively when $[\text{Ca}^{2+}]_{\text{ER}}$ decreases below a threshold of about $150\mu\text{M}$ (Maria Jose' Barrero, 1997). $[\text{Ca}^{2+}]_{\text{ER}}$ in normal cells is reported to be around $350\text{--}500\mu\text{M}$, though this concentration is subject to fluctuation in certain circumstances (Mark J. Henderson, 2015). Though the calcium release from ER to cytoplasm is studied extensively, to the best of our knowledge, none have reported so far the impact of $[\text{Ca}^{2+}]_{\text{ER}}$ on the transient increase of $[\text{Ca}^{2+}]_c$. In this study, we investigated the effect of $[\text{Ca}^{2+}]_{\text{ER}}$ on the transient $[\text{Ca}^{2+}]_c$ increase during the PLC pathway (Putney & Tomita, 2012).

METHODOLOGY

The Virtual Cell software environment (VCELL) (Ion I. Moraru, 2008) was used to develop the kinetic description of the PLC pathway, and the Bio Mode application of VCELL was used to model the cellular compartments. The developed VCELL model is shown in Figure 2. The plasma membrane (pm) and endoplasmic reticulum membrane (erM) divide the space into three compartments: extracellular (ex), cytosol (c) and endoplasmic reticulum (er). The involved species are, Ca^{2+} cytosol (cCa), Ca^{2+} extracellular (exCa), endoplasmic reticulum Ca^{2+} (erCa), initial IP_3 concentration ($\text{IP}_3_{\text{Conc}}$), dynamic IP_3 concentration in cytosol (cIP3), IP_3R (IP_3R), IP_3 bound IP_3R ($\text{IP}_3\text{R_IP}_3$), active IP_3R (active_ IP_3R), inactive IP_3R (inactive_ IP_3R), buffers in cytosol (Buff_high_affi_c), Ca^{2+} bound buffers ($\text{Buff_high_affi_Ca_c}$), Fura2 (Fura2_c), and Ca^{2+} bound Fura2 (Ca_Fura2_c). Leak channels (LCh) transport calcium in between cytosol and ER, depending on the calcium concentration gradient. PMCA and SERCA remove calcium from the cytosol, and IP_3R and Ryn increase calcium in cytosol during the PLC cycle. For the simplicity of the model, GPCR was not included in the developed system. Instead, IP_3 was increased in the cytosol to start the rest of the PLC cycle. Cytosolic IP_3 degradation was also modelled according to previously reported methods (Martin Kruse, 2016).

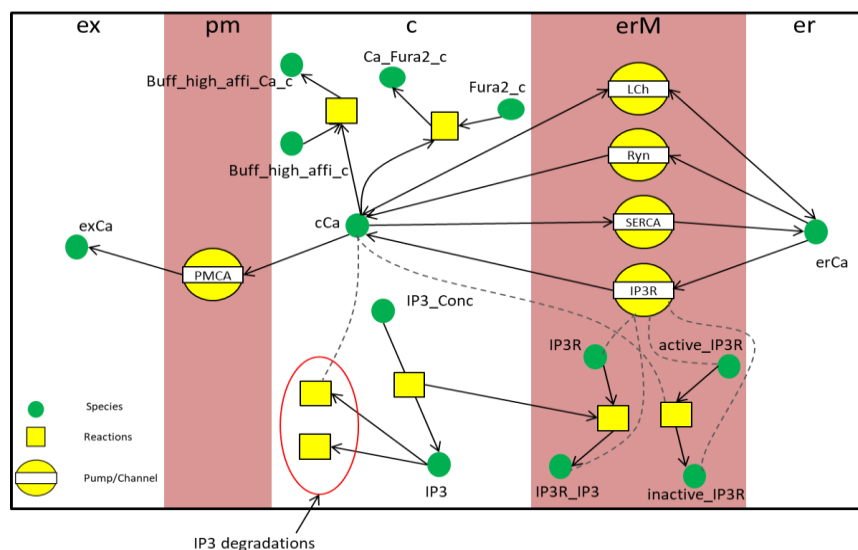


Figure 2: The Modelled PLC pathway. This model was developed with VCELL.

The parameters of the modelled cell (surface area of the membranes and volume of the compartments) were defined as shown in Table 1.

Table 1. Used parameters of compartments and membranes in the model

Parameter	Value	Source
Extracellular volume	250000 μm^3	(Martin Kruse, 2016)
Cytosol volume	6644 μm^3	(Martin Kruse, 2016)
Endoplasmic reticulum volume	1195 μm^3	(Martin Kruse, 2016)
Endoplasmic reticulum membrane surface area	20500 μm^2	(Martin Kruse, 2016)
Plasma membrane surface area	4100 μm^2	(Martin Kruse, 2016)

Previously reported reaction rates (Table 2) and initial concentrations (Table 3) were used in the calculations. Some parameters were chosen according to the experiment to get the best fit in the absence published data. The involved kinetic parameters are shown below and were extracted from the relevant articles listed in Table 2.

1. $\text{erCa} \rightarrow \text{cCa}$ –flux rate of IP_3R ($J_{\text{IP}_3\text{R}}$)

$$J_{\text{IP}_3\text{R}} = a \cdot J_{\text{max}} \cdot \left(1 - \frac{[\text{Ca}^{2+}]_c}{[\text{Ca}^{2+}]_{\text{ER}}}\right) \cdot \left(\frac{h[\text{Ca}^{2+}]_c [\text{IP}_3]}{([\text{Ca}^{2+}]_c + d_{\text{Ca}^{2+}})([\text{IP}_3] + d_{\text{IP}_3})}\right)^3$$

$$h = \left(\frac{\text{Active IP}_3\text{R}}{\text{Active IP}_3\text{R} + \text{Inactive IP}_3\text{R}}\right)^3$$

2. $\text{cCa} \rightarrow \text{erCa}$ – SERCA Flux rate (V_{SERCA})

$$V_{\text{SERCA}} = \frac{k_4 e_0 [\text{Ca}^{2+}]_c^2}{K_m^2 + [\text{Ca}^{2+}]_c^2} = \frac{V_{\text{max}} [\text{Ca}^{2+}]_c^2}{K_m^2 + [\text{Ca}^{2+}]_c^2}$$

3. $\text{erCa} \rightarrow \text{cCa}$ – Ryanodine channel Flux rate (J_{Ryr})

$$J_{\text{Ryr}} = \left(K_1 + \frac{K_2 c^n}{K_d^n + c^n}\right) ([\text{Ca}^{2+}]_{\text{ER}} - [\text{Ca}^{2+}]_c)$$

4. $\text{erCa} \rightarrow \text{cCa}$ – Leak channel Flux rate (V_{Leak})

$$V_{\text{Leak}} = v_{\text{Leak}} ([\text{Ca}^{2+}]_{\text{ER}} - [\text{Ca}^{2+}]_c)$$

5. $\text{active_IP}_3\text{R} \rightarrow \text{Inactive_IP}_3\text{R}$ (IP_3R inactivation, J).

$$J = -(K_D - ([\text{Ca}^{2+}]_c + K_D) \cdot h) \cdot K_{\text{on}}$$

6. $\text{IP}_3\text{Conc} \rightarrow \text{cIP}_3$ (J_{cIP_3})

$$J_{\text{cIP}_3} = \text{IP}_3\text{conc} - e^{-(K_1 + K_2) \cdot t}$$

7. $\text{Fura2_c} + \text{cCa} \rightarrow \text{Ca_Fura2_c}$ – Binding Fura2 with cytosolic

$$\text{Ca}^{2+}(J_{\text{Fura}})J_{\text{Fura}} = K_f \cdot [\text{Fura2}_{\text{cyt}}] \cdot [\text{Ca}^{2+}]_c - K_r \cdot [\text{Ca}^{2+}\text{Fura2}_{\text{cyt}}]$$

$$K_f = \text{speed_Ca_Fura2_c}$$

$$K_r = K_D \cdot K_f$$

8. Buff_high_affi_c + cCa → Buff_high_affi_Ca_c – Ca²⁺ binding with buffers present in the cytosol (J_{Buff})

$$J_{Buff} = K_f \cdot [Ca^{2+}]_c \cdot [buffer_{cyt}] - K_r \cdot [Ca^{2+} \cdot buffer_{cyt}]$$

9. IP₃R + cIP₃ → IP₃R_IP₃ – Cytosolic IP₃ bind with IP₃R receptors in the endoplasmic membrane (J_{IP3R_IP3})

$$J_{IP3R_IP3} = K_f \cdot IP_{3R} \cdot IP_3 - K_r \cdot IP_{3_IP3R}$$

$$K_f = IP_{3_speed} \cdot K_{IP_3_IP3R}$$

$$K_r = IP_{3_speed} \cdot K_{IP_{3R}}$$

10. Cytosolic IP₃ degradation by IP₃ 3-kinase ($Degr_{IP3-3K}$)

$$Degr_{IP3-3K} = v_{3K} \cdot \left(\frac{[Ca_i^{2+}]^4}{[Ca_i^{2+}]^4 + K_D^4} \right) \cdot \left(\frac{[IP_3]}{[IP_3] + K_3} \right)$$

11. Cytosolic IP₃ degradation by the inositol polyphosphate 5-phosphatase (IP-5P) ($Degr_{IP-5P}$)

$$Degr_{IP-5P} = r_{5P} \cdot [IP_3]$$

12. cCa → exCa – Flux rate of cytosolic Ca²⁺ through PMCA pump (V_{PMCA})

$$V_{PMCA} = \frac{V_{PMCA}[Ca^{2+}]_c^2}{K_{PMCA}^2 + [Ca^{2+}]_c^2}$$

Table 2. Rate constants and parameters

Parameter Name	Parameter	Value	Rationale For Parameter
Density of IP ₃ R in the system	α	1.0	(Nicholas Hernjak, 2005)
Maximum rate of IP ₃ binding	I_{max}	80.0 μM.s ⁻¹	(Martin Kruse, 2016)
IP ₃ R and Ca ²⁺ binding constant	$d_{Ca^{2+}}$	0.2 μM	(Martin Kruse, 2016)
IP ₃ R and IP ₃ binding constant	d_{IP3}	0.1 μM	(Martin Kruse, 2016)
Amplitude of SERCA pump intake	V_{max}	7.2 μM.s ⁻¹	Fit to the model
SERCA pump binding constant	K_m	0.24 μM	(Jung Min Han, 2017)
Forward reaction rate constant of Ryanodine	K_1	5×10 ⁴ s ⁻¹	Fit to the model
Reverse reaction rate constant of ryanodine	K_{-1}	0.005 s ⁻¹	Fit to the model
Dissociation constant of ryanodine	K_d	0.58 μM	(James Keener, 2009)

Leak constant	v_{Leak}	0.0032 s ⁻¹	Fit to the model
Inactivation rate constant	K_D	0.2 μM	(Martin Kruse, 2016)
Activation rate constant	K_{on}	2.7 molecules.μm ⁻² . s ⁻¹ .μM ⁻¹	(Martin Kruse, 2016)
Forward reaction rate constant for IP ₃ apply	K_1	0.2 s ⁻¹	Fit to the model
Reverse reaction rate constant for IP ₃ apply	K_2	0.1 s ⁻¹	Fit to the model
Conversion factor of Fura2	$speed_Ca_Fura2_c$	0.2 s ⁻¹ .μM ⁻¹	Fit to the model
Dissociation constant for Fura2	K_D	0.144 μM	Fit to the model
Forward reaction rate constant for buffer binding	K_f	10.0 s ⁻¹ .μM ⁻¹	(Martin Kruse, 2016)
Reverse reaction rate constant for buffer binding	K_r	3.8 s ⁻¹	Fit to the model
IP ₃ and IP ₃ R binding constant	$K_{IP_3-IP_3R}$	0.1 μM	Fit to the model
Dissociation constant of IP ₃	K_{IP_3R}	0.5 μM	Fit to the model
IP ₃ affinity of IP ₃ - 3K	K_3	1.0 μM	Franziska Oschmann, 2017)
Ca ²⁺ affinity of IP ₃ - 3K	K_D	0.7 μM	(Franziska Oschmann, 2017)
Maximum degradation rate of IP ₃ by IP ₃ - 3K	v_{3K}	2.0 μM. s ⁻¹	(Franziska Oschmann, 2017)
Maximum degradation rate of IP ₃ by IP- 5K	r_{5p}	0.4 s ⁻¹	(Franziska Oschmann, 2017)
Amplitude of PMCA pump intake	V_{PMCA}	0.2 μM. s ⁻¹	Fit to the model
PMCA pump binding constant	K_{PMCA}	0.45 μM	(Jung Min Han, 2017)

Table 3. Initial concentrations of species.

Species	Initial Condition
erCa	350 μM^*
cCa	0.1 μM
cIP ₃	0.0 μM
IP ₃ _Conc	5.0 μM
Buffer_C	12.0 μM
Buffer_Ca_C	0.0 μM
Fura2_C	3.0 μM
Ca_Fura2_C	0.0 μM
Inactive_IP ₃ R	0.0 molecules. μm^{-2}
Active_IP ₃ R	1.0 molecules. μm^{-2}
IP ₃ R	400.0 molecules. μm^{-2}
IP ₃ R_IP ₃	0.0 molecules. μm^{-2}

**The model was developed at 350 μM . The concentration was changed according to the experiment.*

RESULTS AND DISCUSSION

The initial cytosolic IP₃ concentration was set to 5 μM . When IP₃ is released to the cytosol, it binds with the IP₃R present in the endoplasmic reticulum membrane while undergoing degradation. Upon binding with IP₃, the IP₃R's start to release Ca²⁺ ions from the ER lumen, increasing Ca²⁺ ions in the cytosol. The perturbation to the equilibrated system by IP₃ was started at 60s (allowing the system to reach initial equilibration in first 60 s) and stopped at 70s. There are two IP₃ degradation pathways: IP₃-3 Kinase and inositol polyphosphate-5-phosphatase. After a certain time period from the activation, IP₃R channels begin to deactivate (Taylor & Tovey, 2010). The local increase of Ca²⁺ is sensed by ryanodine receptors, activating them to transport a large amount of ER Ca²⁺ ions to the cytosol. As a result, a global increase of Ca²⁺ in the cytosol can be observed. Figure 3a shows the cytosolic calcium increase with IP₃ perturbation at 60 s when the ER calcium concentration is 350 μM . The sudden increase of free Ca²⁺ ions in the cytosol activates many calcium regulatory pathways. Cytosolic buffers and calcium sensitive dyes (e.g., Fura2) start to scavenge excessive calcium, helping the cytosol to bring the concentration of calcium down. PMCA and SERCA pumps start to work when the cytosolic Ca²⁺ concentration passes their threshold. As a result of all the major Ca²⁺ regulating processes mentioned above, cytosolic Ca²⁺ concentration comes to its normal concentration of 0.1 μM . As the Ca²⁺ concentration increases in the cytosol, the ER Ca²⁺ concentration starts to decrease (Figure 3b).

Before introducing IP₃ to the cytosol, the ER lumen Ca²⁺ concentration is higher than the cytosolic Ca²⁺ concentration. The calcium outflow from the leak channels depends on the ER Ca²⁺ concentration. Initially, leak channels and SERCA pumps work collaboratively to maintain the cytosolic calcium concentration at 0.1 μM . When the simulation starts at time zero, the Ca²⁺ ion concentration in the ER lumen decreases before it equilibrates with the cytosol. The main reason is

the binding of buffers (12 μ M) and Fura2 (3 μ M) with cytosolic Ca^{2+} which lowers the cytosolic calcium concentration. To compensate for the loss of calcium from the cytosol, the ER releases more calcium to the cytosol via leak channels, and finally SERCA and leak channels collectively bring the system to equilibrium. This takes approximately 40 s from the start of the simulation. Therefore, IP_3 perturbation was triggered at 60 s, letting the system stay in an equilibrated condition for 20 s.

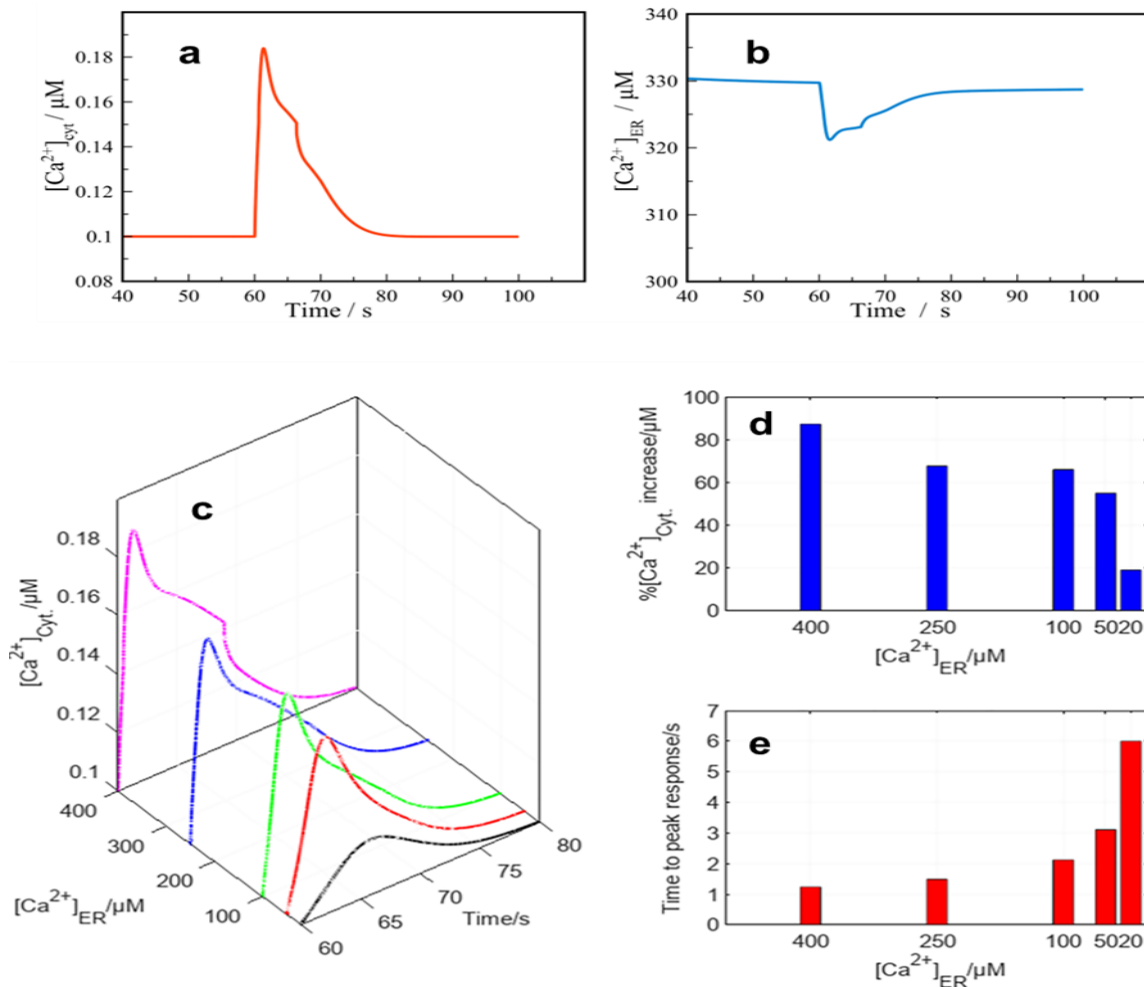


Figure 3. (a) Cytosolic Ca^{2+} concentration variations with the time when $[\text{Ca}^{2+}]_{\text{ER}}$ is 350 μM . (b) ER Ca^{2+} concentration variation with time when $[\text{Ca}^{2+}]_{\text{ER}}$ is 350 μM . (c) $[\text{Ca}^{2+}]_{\text{c}}$ variation at different $[\text{Ca}^{2+}]_{\text{ER}}$ (purple=400 μM , blue=250 μM , green=100 μM , red= 50 μM and black=20 μM). (d) Percentage increment of $[\text{Ca}^{2+}]_{\text{c}}$ with different $[\text{Ca}^{2+}]_{\text{ER}}$. (e) Time to peak response at different $[\text{Ca}^{2+}]_{\text{ER}}$.

Reported experimental calcium released at a show different peak heights and times to peak response though the other experimental conditions are kept constant. This observation can be explained in a few ways. In one possible approach, cells contain different concentrations of calcium ions in their ER lumen, which affect the peak response and time to peak response. After the successful development of the model at a concentration of ER calcium of 350 μM , we studied the impact of ER Ca^{2+} concentrations on the transient change of cytosolic Ca^{2+} concentrations to test our

hypothesis. Simulations were done at different ER lumen Ca^{2+} concentrations: 400 μM , 250 μM , 100 μM , 50 μM , and 20 μM . The simulated cytosolic calcium responses are shown in Figure 3c. The data confirms the dependency of $[\text{Ca}^{2+}]_c$ on the $[\text{Ca}^{2+}]_{\text{ER}}$. The percentage increase of the response from the base level and the time to reach the peak response is analyzed by using the simulated data (Figures 3d and 3e). The activation of IP_3R by the introduction of IP_3 at 60 s increased the $[\text{Ca}^{2+}]_c$ by 90% within 2s at $[\text{Ca}^{2+}]_{\text{ER}} = 400\mu\text{M}$. When the $[\text{Ca}^{2+}]_{\text{ER}}$ was decreased, the transient peak of $[\text{Ca}^{2+}]_c$ evoked by IP_3 also decreased non-linearly and reached only a ~20% increase in 6s for $[\text{Ca}^{2+}]_{\text{ER}} = 20\mu\text{M}$. It is evident that the percentage decrease of the response is low until the ER lumen calcium concentration reaches 50 μM . However, there is a significant drop of the $[\text{Ca}^{2+}]_c$ when the ER lumen calcium concentration changes from 50 μM to 20 μM . The time to reach the peak response displayed a nice multi-order exponential increase with the concentration change from 400 μM to 20 μM . Though there are several possible explanations for the observation of diverse $[\text{Ca}^{2+}]_c$ responses in the PLC pathway, we tested one major contributor for the $[\text{Ca}^{2+}]_c$ response, ER lumen calcium concentration. This model confirms the profound impact of the Ca^{2+} concentration of ER lumen on the cytosolic transient calcium response during the PLC pathway.

CONCLUSION

According to our results, the increase of the $[\text{Ca}^{2+}]_c$ and time to peak response from the addition of IP_3 in the PLC pathway depend on the $[\text{Ca}^{2+}]_{\text{ER}}$. Therefore, we suggest that in any study performed to investigate the cytosolic calcium signaling during the PLC pathway, it is necessary to determine and report the $[\text{Ca}^{2+}]_{\text{ER}}$ to correctly interpret the experimental observations.

ACKNOWLEDGEMENT

This work was supported by Grant ASP/01/RE/SCI/2017/18 (University of Sri Jayewardenepura). The corresponding author wishes to thank Prof. Nevin Lambert, Augusta University, Augusta, GA, USA.

REFERENCES

- Franziska Oschmann, K. M., Evelyn Jungnickel, Klaus Obermayer. (2017). Spatial separation of two different pathways accounting for the generation of calcium signals in astrocytes. *PLOS Computational Biology*, 1-25.
- Ion I. Moraru, J. C. S., Boris M. Slepchenko, Michael Blinov, Frank Morgan, Anuradha Lakshminarayana, Fei Gao, Ye Li, and Leslie M. Loew. (2008). The Virtual Cell Modeling and Simulation Software Environment. *IET Syst Biol*, 2, 352–362.
- James Keener, J. S. (2009). *Mathematical Physiology*.: Springer.
- Jung Min Han, A. T., Vivien Kirk, James Sneyd. (2017). A mathematical model of calcium dynamics in HSY cells. *PLOS Computational Biology*.
- Kanayo Satoh, K. M., Toru Matsu-ura, Masahiro Enomoto, Hideki Nakamura, Takayuki Michikawa. (2011). Highly Cooperative Dependence of Sarco/Endoplasmic Reticulum Calcium ATPase (SERCA) 2a Pump Activity on Cytosolic Calcium in Living Cells. *BIOLOGICAL CHEMISTRY*, 286, 20591–20599. doi: 10.1074/jbc.M110.204685

Lisa A. Selbie, S. J. H. (1998). G protein-coupled receptor cross-talk: the fine-tuning of multiple receptor-signalling pathways. *19*.

Maria Jose´ Barrero, M. M., Javier Alvarez. (1997). Dynamics of [Ca²⁺] in the Endoplasmic Reticulum and Cytoplasm of Intact HeLa Cells. *BIOLOGICAL CHEMISTRY*, *272*, 27694–27699.

Mark J. Henderson, H. A. B., Christopher A. Werley, Stefano Boccoardo, Leslie R. Whitaker, Xiaokang Yan, Graham T. Holt, Eric R. Schreiter, Loren L. Looger, Adam E. Cohen, Douglas S. Kim, Brandon K. Harvey. (2015). A Low Affinity GCaMP3 Variant (GCaMP_{er}) for Imaging the Endoplasmic Reticulum Calcium Store. *PLOS ONE*. doi: 10.1371/journal.pone.0139273

Martin Kruse, O. V., Alexis Traynor-Kaplan, XBertil Hille. (2016). Dynamics of Phosphoinositide Dependent Signaling in Sympathetic Neurons. *Neuroscience*, *36*(4), 1386–1400.

Michael J. Berridge, M. D. B., H. Llewelyn Roderick. (2003). CALCIUM SIGNALLING: DYNAMICS, HOMEOSTASIS AND REMODELLING. *NATURE*, *4*, 517-529.

Nicholas Hernjak, B. M. S., Kathleen Fernald, Charles C. Fink, Dale Fortin, Ion I. Moraru, James Watras, and Leslie M. Loew. (2005). Modeling and Analysis of Calcium Signaling Events Leading to Long-Term Depression in Cerebellar Purkinje Cells. *Biophysical*, *89*, 3790–3806.

Putney, J. W., & Tomita, T. (2012). Phospholipase C Signaling and Calcium Influx. *Adv Biol Regul*, *52*, 152-164.

Raymond C. Stevens, V. C., Vsevolod Katritch, Ruben Abagyan, Peter Kuhn, Hugh Rosen, Kurt Wüthrich. (2014). GPCR Network: a large-scale collaboration on GPCR structure and function. *PMC*, 25–34. doi: 10.1038/nrd3859.

Rosario Rizzuto, S. M., Massimo Bonora, Paola Aguiari, Angela Bononi, Diego De Stefani, Carlotta Giorgi, Sara Leo, Alessandro Rimessi, Roberta Siviero, Erika Zecchini, Paolo Pinton. (2009). Ca²⁺ transfer from the ER to mitochondria: When, how and why. *Biochimica et Biophysica Acta*, *1787*, 1342–1351.

Taylor, C. W., & Tovey, S. C. (2010). IP₃ Receptors: Toward Understanding Their Activation. *Cold Spring Harb Perspect Biol.*, *2*, 1-22.

Wojcikiewicz, R. J. H. (2012). Inositol 1,4,5-trisphosphate receptor degradation pathways. *1*, 126–135. doi: 10.1002/wmts.4

Yamauchi T, K. J., Ito Y, Tsuchida A, Yokomizo T, Kita S, Sugiyama T, Miyagishi M, Hara K, Tsunoda M, Murakami K, Ohteki T, Uchida S, Takekawa S, Waki H, Tsuno NH, Shibata Y, Terauchi Y, Froguel P, Tobe K, Koyasu S, Taira K, Kitamura T, Shimizu T, Nagai R, Kadowaki T (2003). Cloning of adiponectin receptors that mediate antidiabetic metabolic effects. *NATURE*, *423*, 762–769. doi: 10.1038/nature01683.

Mathematical Modelling of Step Shape Bed Forms Generated by Turbidity Currents without incorporating the Wave Entrainment Impact

H.M.K.N.Herath,* S.D.Sirithunge and D.D.Dias

Department of Civil Engineering, Faculty of Engineering, University of Peradeniya, Sri Lanka

ABSTRACT

Froude supercritical flow over an erodible bed is inherently unstable. Such supercritical flows over a steep moveable bed may create bedforms. The most common kind of such bedforms are the antidunes. They are short wave bedforms that interact with the flow and are most commonly observed to be migrating upstream. In some cases, these upstream migrating antidunes give way to more stable long waves, bounded by hydraulic jumps in the flow above them, which stabilizes the flow and morphodynamics. This long wave manifestation is called 'cyclic steps.' Cyclic steps constitute a characteristic long wave bed form of Froude-supercritical shallow flow over an erodible bed. These bed forms commonly occur in regions with high gradient and slope breaks. Studies have been carried out to understand this phenomenon with the use of mathematical modelling techniques and some field observations are also reported in the literature. This study investigates the formation of cyclic steps in sub-aqueous environments, without incorporating the wave entrainment using an idealized mathematical model. A model has been developed preserving the essential physics of the system, incorporating the dominant mechanisms governing morphodynamic process.

Keywords: *Cyclic steps, entrainment effect, idealization*

1. Introduction

Cyclic step can be categorized into two main folds based on the formation mechanism. They are transportational cyclic steps and purely erosional cyclic steps. The steps termed as "transportational" because they are associated with spatially varying patterns of erosion of sediment into and deposition from suspension. Purely erosional cyclic step can occur in the case of flow over a cohesive bed or bedrock. Turbidity currents are the mainly influence for the formation of cyclic steps in sub-aqueous environments. They are self-generated currents. Supercritical turbidity currents are thought to be common in high gradient submarine canyons and channels of the continental slope (Fildani et al., 2006). Also, subcritical turbidity currents are common in lower gradient channels and depositional lobes of the continental rise and basin floor. Entrainment is the transport of fluid across an interface between two bodies of fluid by a shear induced turbulent flux. This model developed to explain the phenomenon of cyclic step formation without incorporating the wave entrainment impact as the impact due to wave entrainment has been studied in the previous research attempts (Dias D.D, et. al, 2011). Field observations, mathematical based approaches are reported in literature in relation to this bed form evolution yet the sensitivity of the incorporation of wave entrainment impact has not been addressed in previous research interventions.

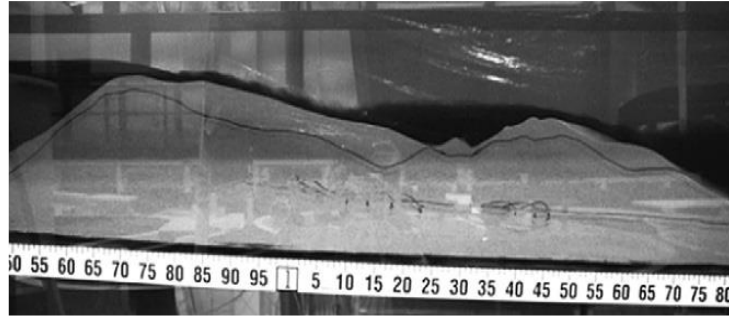


Figure 1: Cyclic steps as modeled in the experiments.
Dark shades denote the flow, which is from left to right (Taki K, *et.al.*, 2005)

METHODOLOGY

Governing equations

The layer averaged continuity equation of turbidity current (Fildani *et al.*, 2006) was developed to describe the mass continuity of the turbidity current,

$$\frac{\partial \tilde{h}}{\partial \tilde{t}} + \frac{\partial \tilde{U} \tilde{h}}{\partial \tilde{x}} = e_w \tilde{U} \quad (1)$$

The movement of the turbidity current is described by the layer averaged momentum equation (Dias *et al.*, 2011) of the form

$$\frac{\partial \tilde{U}}{\partial \tilde{t}} + \tilde{U} \frac{\partial \tilde{U}}{\partial \tilde{x}} = -\frac{Rg\tilde{h}}{2} \frac{\partial \tilde{C}}{\partial \tilde{x}} - Rg\tilde{C} \frac{\partial \tilde{h}}{\partial \tilde{x}} - Rg\tilde{C} \frac{\partial \tilde{\eta}}{\partial \tilde{x}} + Rg\tilde{C}S - \frac{\tilde{\tau}_b}{\rho \tilde{h}} \quad (2)$$

The Exner equation of sediment continuity (Dias *et al.*, 2011), which depicts the bottom evolution due to positive interplay between the turbidity current and the erodible sea floor is given by,

$$(1 - \lambda_p) \frac{\partial \tilde{\eta}}{\partial \tilde{t}} = v_s (\tilde{D} - \tilde{E}) \quad (3)$$

The dispersion equation of suspended sediment (Fildani *et al.*, 2006) is defined by

$$\frac{\partial \tilde{C} \tilde{h}}{\partial \tilde{t}} + \frac{\partial \tilde{U} \tilde{C} \tilde{h}}{\partial \tilde{x}} = v_s (\tilde{E} - \tilde{D}) \quad (4)$$

Here \tilde{t} is the time, \tilde{x} is the stream wise coordinate, \tilde{U} is the layer-averaged velocity in the \tilde{x} direction, \tilde{h} is the layer thickness, \tilde{C} is the layer-averaged suspended sediment concentration, $\tilde{\eta}$ is the bed elevation referenced to the slope of S , R is the submerged specific gravity ($= 1.65$), g is the gravity acceleration ($= 9.8 \text{ m/s}^2$), ρ is the density of sea water (1025 kg/m^3), $\tilde{\tau}_b$ is the bed shear stress, \tilde{E} is

the entrainment rate of suspended sediment from the bottom, \tilde{D} is the deposition rate of suspended sediment onto the bed, v_s is the falling velocity of suspended sediment. \tilde{E} , \tilde{D} and the bed shear stress parameters are expressed by the following equations:

$$\tilde{E} = \begin{cases} a \left(\frac{\tilde{\tau}_b}{\tilde{\tau}_{th}} - 1 \right)^n & \text{when } \tilde{\tau}_b \geq \tilde{\tau}_{th} \\ 0 & \text{when } \tilde{\tau}_b < \tilde{\tau}_{th} \end{cases}, \quad \tilde{D} = r_o \tilde{C}, \quad \tilde{\tau}_b = \rho c_D \tilde{U}^2 \quad (5. a, b, c)$$

Also, a and n are empirical constants determined by experiments and τ_{th} is the critical bed shear stress below which no entrainment takes place; r_o is the ratio between the suspended sediment concentration near the bed and layer average suspended sediment concentration (for simplicity, it is assumed that r_o is equal to unity); c_D is the drag coefficient, which is a constant.

Idealized Mathematical Model Development

In this research, it was assumed that the turbidity current just drags on the erodible bed and, subsequently, a bed form evolves. Though there is definitely an expected mixing of two media, in this research its impact was neglected. It was assumed that the ocean bed and turbidity current behave independently. Therefore, it was assumed that the entrainment rate (e_w) was zero. Most of the previous research has been carried out in steep erodible sea beds and carved canyons (e.g., cyclic steps and related supercritical bed forms in Western North America (Kostic et al., 2016), where in most instances, the length of the canyon was significantly larger than its width.

For the simplicity, it was assumed that the width of the turbidity current is constant and the variations taking place along the width direction were assumed to be negligible relative to the length of the turbidity current. Also, this study focuses only along the turbidity current; hence the model is 1D. The analysis was done focusing on the self-preserving quasi-steady step shape migrating upstream without changing its shape over a single wavelength.

Non-dimensionalization

Dimensional partial differential equations are difficult to handle in linearization and it is complicated

$$\tilde{U} = \tilde{U}_c U, \quad \tilde{C} = \tilde{C}_c C, \quad \tilde{h} = \tilde{H}_c h, \quad \tilde{\eta} = \tilde{H}_c \eta, \quad \tilde{E} = \tilde{E}_c E, \quad \tilde{x} = \frac{\tilde{H}_c}{c_D} x, \quad \tilde{D} = \tilde{D}_c D$$

$$\tilde{t} = \left[\frac{(1 - \lambda_p) \tilde{H}_c}{v_s \tilde{D}_c} \right] t$$

to develop a relationship between dimensional parameters. Therefore, before solving the set of equations, the governing equations have to be linearized and simplified based on the assumptions. Dimensional governing equations were turned into non-dimensional form with the incorporation of normalization as stated below.

In the normalization specified above, $\tilde{U}_c, \tilde{H}_c, \tilde{C}_c, \tilde{E}_c$, and \tilde{D}_c are the velocity, flow depth, suspended sediment concentration, entrainment rate from the bottom, and deposition rate from suspension at the Richardson critical point, respectively. Adopting the defined normalization, normalized governing equations can be written in the form

$$\alpha \frac{\partial h}{\partial t} + \frac{\partial U h}{\partial x} = 0 \quad (7)$$

$$\alpha \frac{\partial U}{\partial t} + U \frac{\partial U}{\partial x} = -\frac{h}{2} \frac{\partial C}{\partial x} - C \frac{\partial h}{\partial x} - C \frac{\partial \eta}{\partial x} + \sigma C - \frac{U^2}{h} \quad (8)$$

$$\frac{\partial \eta}{\partial t} = C - \gamma E, \quad \alpha \beta \frac{\partial C h}{\partial t} + \beta \frac{\partial U C h}{\partial x} = \gamma E - C \quad (9), (10)$$

In here,

$$\alpha = \frac{v_s \tilde{D}_c}{(1 - \lambda_p) c_D \tilde{U}_c}, \quad \beta = \frac{c_D \tilde{U}_c \tilde{C}_c}{v_s \tilde{D}_c}, \quad \sigma = \frac{S}{c_D}, \quad \gamma = \frac{\tilde{E}_c}{\tilde{D}_c}. \quad (11.a,b,c,d)$$

For simplicity it was assumed that; $\frac{R g \tilde{C}_c \tilde{H}_c}{\tilde{U}_c^2} = 1$ and $r_0 = 1$. The α terms are assumed to be small enough to be neglected (Kostic S, et. al, 2006, Dias et al. 2011). For dropping terms of time derivatives, a quasi-steady state of the cyclic step formation mechanism was assumed. With these assumptions normalized governing equations were simplified in the forms given in equation 12 – 15.

$$\frac{\partial U h}{\partial x} = 0, \quad U \frac{\partial U}{\partial x} = -\frac{h}{2} \frac{\partial C}{\partial x} - C \frac{\partial h}{\partial x} - C \frac{\partial \eta}{\partial x} + \sigma C - \frac{U^2}{h} \quad (12), (13)$$

$$\beta \frac{\partial U C h}{\partial x} = \gamma E - C \quad (14)$$

If the unsteady terms in the Exner equation are dropped, the bed evolution process would not be captured by the model; hence the unsteady terms in Exner equation were preserved without omitting under the logic within the quasi steady assumption.,

$$\frac{\partial \eta}{\partial t} = C - \gamma E \quad (15)$$

Coordinate Transformation

If part of a cyclic step is considered, it changes with time. This implies a migration of the step, where steps migrate upstream at constant speed of f without changing form, and without net aggradation or degradation averaged over one wavelength, under the considered situation. Therefore, to capture this upstream migration of a step, a moving coordinate system was introduced to represent the time derivate, where migration speed is denoted by f .

$$\bar{x} = x + ft$$

Applying this coordinate transformation to unsteady governing equations,

$$\frac{\partial U h}{\partial \bar{x}} = 0, \quad U \frac{\partial U}{\partial \bar{x}} = -\frac{h}{2} \frac{\partial C}{\partial \bar{x}} - C \frac{\partial h}{\partial \bar{x}} - C \frac{\partial \eta}{\partial \bar{x}} + \sigma C - \frac{U^2}{h} \quad (17), (18)$$

$$\beta \frac{\partial U C h}{\partial \bar{x}} = \gamma E - C, \quad \frac{\partial \eta}{\partial \bar{t}} + f \frac{\partial \eta}{\partial \bar{x}} = C - \gamma E \quad (19), (20)$$

The unsteady terms in the final set of linearized governing equations were dropped; accordingly the time derivatives in the linearized, simplified Exner equation were omitted and “ \sim ” marks was removed for the simplicity of representation. Finally, the partial derivatives were replaced by total derivatives.

$$\frac{dU h}{dx} = 0, \quad U \frac{dU}{dx} = -\frac{h}{2} \frac{dC}{dx} - C \frac{dh}{dx} - C \frac{d\eta}{dx} + \sigma C - \frac{U^2}{h} \quad (21), (22)$$

$$\beta \frac{dU C h}{dx} = \gamma E - C, \quad f \frac{d\eta}{dx} = C - \gamma E \quad (23), (24)$$

The equations 25 – 27 were obtained by manipulating the equations 21 – 24.

$$\frac{dU}{dx} = \frac{\left[\frac{C}{f} - \frac{1}{2\beta U} \right] (\gamma E - C) + \sigma C - \frac{U^2}{h}}{U - \frac{Ch}{U}} \quad (25)$$

$$\frac{dC}{dx} = \frac{\gamma E - C}{\beta U h} \quad (26)$$

$$\frac{dh}{dx} = \frac{\left[\frac{Ch}{f} - \frac{h}{2\beta U} \right] (\gamma E - C) + \sigma Ch - U^2}{U^2 - Ch} \quad (27)$$

When $U = 1, C = 1, h = 1, U - \frac{Ch}{U}$ is equal to zero, creating a singularity in the expression. Then to neutralize the effect of the particular singularity, the numerator of the equation 25 was equated to zero, which results in

$$\left[\frac{C}{f} - \frac{1}{2\beta U} \right] (\gamma E - C) + \sigma C - \frac{U^2}{h} = 0 \quad (28)$$

This creates a function for the moving velocity f as shown in the equation 29.

$$f = \frac{2\beta(\gamma - 1)}{(\gamma - 2\beta\sigma + 2\beta - 1)} \quad (29)$$

Ultimately the following is produced:

$$\frac{d\eta}{dx} = \frac{C - \gamma E}{f} \quad (30)$$

Boundary Condition

To solve the governing equations, first the problem was considered as a two-point boundary value problem. Mainly this is composed of four differential equations, and a shooting method incorporating the Newton-Raphson scheme was used to solve the problem, which has been successfully used in the research done with the incorporation of entrainment impact (Dias et al. 2011). Accordingly, the solving process was started at the vicinity of the Richardson critical point to avoid the singularities and the calculations were performed towards the upstream and downstream ends until the specified boundary conditions were met. Figure 2 shows the Conceptual Diagram of a turbidity current and the important points to be considered in the solving process

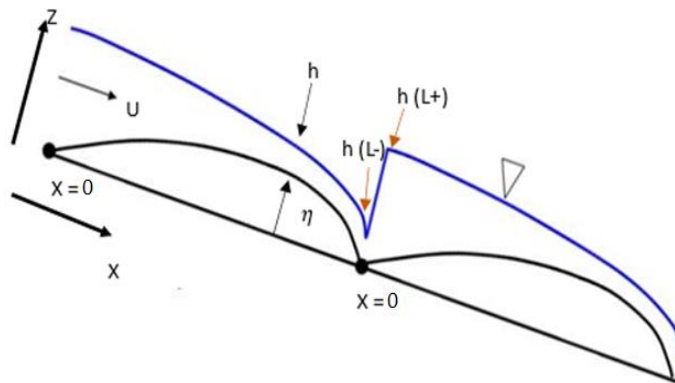


Figure 2: Conceptual diagram of a turbidity current

Using momentum conservation and continuous mass between the upstream and downstream of the hydraulic jump, it can be written as,

$$U^2(L-)h(L-) + \frac{1}{2}C(L)h^2(L-) = U^2(L+)h(L+) + \frac{1}{2}C(L)h^2(L+) \quad (31)$$

Suspended sediment concentration can be considered as continuous between the upstream and downstream side of the hydraulic jump. Therefore, $C(L-) = C(L+) = C(L)$ was obtained (Dias et al. 2011). The mass of the turbidity current was also continuous between the upstream and downstream of the hydraulic jump. Therefore, $U(L-)h(L-) = U(L+)h(L+) = q(L)$. At the

downstream end of the hydraulic jump, the bed eroded until the velocity reduces to a threshold velocity, and at $x = L$ the velocity was the conjugate velocity, leading to an equation depicted as $U(0+) = U(L+) = U_{th}$ (Parker G., 2004). Also, $U(L-)$ can be taken from equation as.

$$\frac{U(L-)}{U_{th}} = \frac{1 + \left[1 + 8 \frac{U_{th}^3}{q(L)C(L)}\right]^{1/2}}{\frac{4U_{th}^3}{q(L)C(L)}} \quad (32)$$

Bed elevation reference to slope is taken as

$$\eta(0) = \eta(L) = 0 \quad (\text{Dias et al. 2011 and Parker G. 2004}). \quad (33)$$

$\eta = 0$ at the downstream end of the step. Then the concentration can be written as

$$C(L) = \frac{U_{th}C(0)h(0+)}{U(L-)h(L-)} = \frac{U_{th}C(0)h(0+)}{q(L)} \quad (34)$$

Equation 35 can be derived by using equations 33 and 34.

$$\frac{U(L-)}{U_{th}} = \frac{1 + \left[1 + 8 \frac{U_{th}^3}{C(0)h(0+)}\right]^{1/2}}{\frac{4U_{th}^3}{C(0)h(0+)}} \quad (35)$$

And it can be further reduced to equation 36.

$$\frac{U(L-)}{U_{th}} = \frac{1}{4} Ri(0+) \{1 + [1 + 8 Ri^{-1}(0+)]^{1/2}\} \quad (36)$$

Here Ri is the Richardson number. Also two equations were obtained for critical layer thickness (\tilde{H}_c) and suspendability (β), respectively. Those equations are as follows,

$$\tilde{H}_c = \sqrt[3]{\frac{\tilde{Q}^2}{Rg\tilde{C}_c}}, \quad \beta = \frac{C_D R^{2/3} g^{2/3} \tilde{C}_c^{5/3}}{\tilde{v}_s \tilde{Q}^{1/3}} \quad (37), (38)$$

Here Q is the total discharge per unit width. Finally, the ranges of prominent parameters to be used in the solving process were obtained based on the previous research outcomes (Dias et al., 2011, Kostic et al., 2006). Those parameters are $C_D = 0.002 - 0.02$, $\tilde{C}_c = 0.01 - 0.3$, $\tilde{v}_s = 0.001 - 0.01$ m/s, $\tilde{Q} = 0.1 - 10$ m²/s, $\beta = 0.00028 - 37$.

RESULTS AND DISCUSSION

Typical values of parameters, variations of governing parameters, and comparison of the results with previous research outcomes are discussed here. C_D , σ and λ were obtained as functions of suspendability. Here λ is wavelength. From those relationships (equations 37 and 38), it was observed that when the suspendability increased, the wavelength was also increased proportionately. Typical values for drag coefficient, suspendability, and σ were 0.005, 0.1, and 2, respectively (Dias *et al.*, 2011), and the average slope of the ocean floor at the cyclic step generated site was observed as 0.01 (Fildaniet *al.*, 2006) at Shepard Meander.

Figures 3, 4, 5, and 6 depict the distribution of layer averaged velocity, layer thickness, suspended sediment concentration, and bed elevation, respectively, over one step wavelength when the conditions, described above under the boundary conditions, are acceptable. It is shown in Figure 3 that, in the up-stream side, the flow is subcritical, and it abruptly accelerates towards the downstream end and becomes a supercritical flow. Therefore, the Richardson number is larger than one in the upstream region and lower than one in the downstream region. It is shown in Figure 4 that the suspended sediment concentration decreases in the upstream part of the step where the flow is subcritical, and the concentration increases in the downstream part where the flow is supercritical. These results tally with the assumptions made in the methodology section where concentration was presumed as continuous through the hydraulic jump.

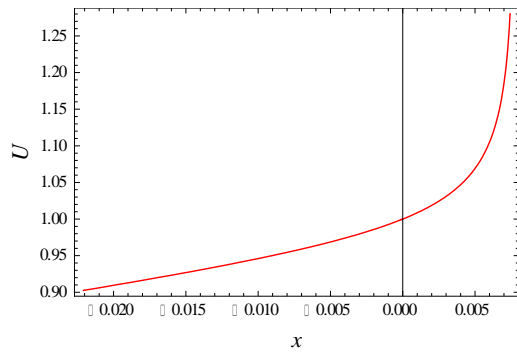


Figure 3: Layer averaged velocity

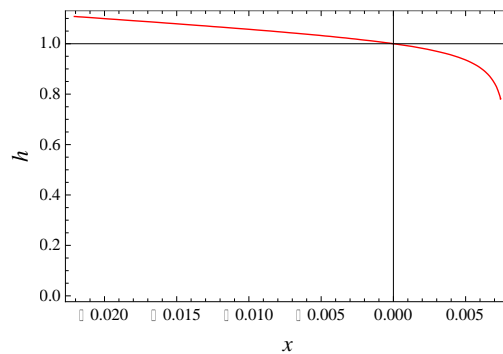


Figure 4: Layer thickness

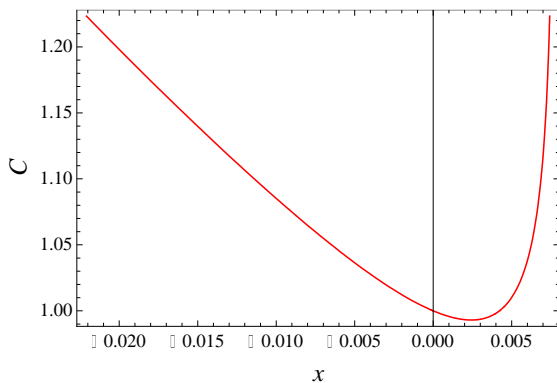


Figure 5: Layer averaged suspended

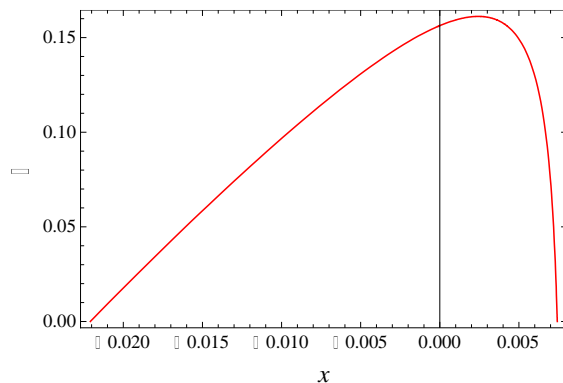


Figure 6: Bed elevation

sediment Concentration

Bed forms are bounded upstream and downstream by a hydraulic jump. The slow flow just downstream of the hydraulic jump causes net deposition, swift flow just upstream of the hydraulic jump causes net erosion. As a result, it is possible for the steps to migrate upstream without changing their form, and the net bed aggradation or degradation over a single wavelength is approximately zero. The upstream migrating step shape is shown in Figure 6. The conceptual diagram of upstream migrating steps is shown in Figure 7.

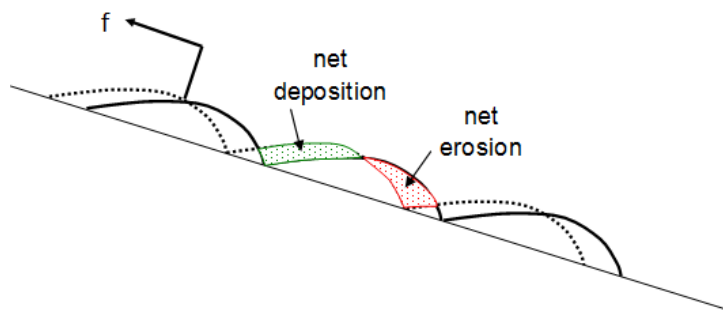


Figure 7: Conceptual diagram of upstream migrating steps. Redraft from Parker, 2006

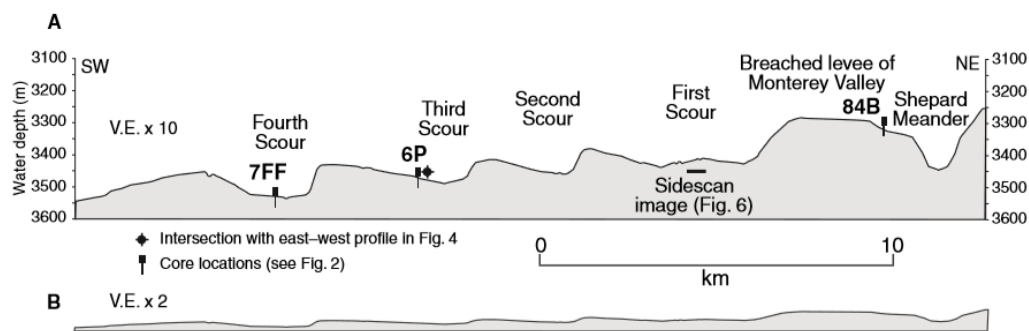


Figure 8 Cyclic steps observed in ocean (Fildani et al. 2006)

The Monterey East system in Shepard Meander is formed by large scale sediment waves on the outside of the Shepard Meander. A giant scour feature is observed using high resolution seismic reflection techniques as shown in the Figure 3.6. This marine environment process and its features are similar to the cyclic step generated by the model in this analysis. The series of cyclic step observed by Fildani (2006), is shown in the Figure 8.

According to the Figure 8 the height and length of the steps are approximately 90 m and 3300 m, respectively. So, the cyclic steps observed in the ocean satisfy the long wave assumptions. For the modeling of the cyclic steps it was assumed that these bed forms were generated under the sub-aqueous conditions. This assumption was confirmed by the abrupt bed elevation increment in the generated step as shown in Figure 6, unlike the cyclic steps generated by sub-aerial settings.

Subsequence cyclic steps are long waves, so that the wavelength is larger than the layer thickness in some order of magnitude. Since the drag coefficient is assumed to be 0.005, the wavelength plotted in the Figure 3.4 is more than forty times larger than the critical layer thickness. So, the long wave assumption is satisfied by this model, as in field observations.

Figures 9, 10, and 11 depict the variation of layer-averaged velocity with different suspendability(β) and ratio between bottom entrainment and deposition (γ) values. When the suspendability increases and reaches a higher number of values from 10 to 37, the step shape cannot form. However when γ is also increased simultaneously with suspendability, the shape of the cyclic step is observed. Therefore, it was found that there is an approximately linear relationship between the suspendability and γ , when the β goes to higher values.

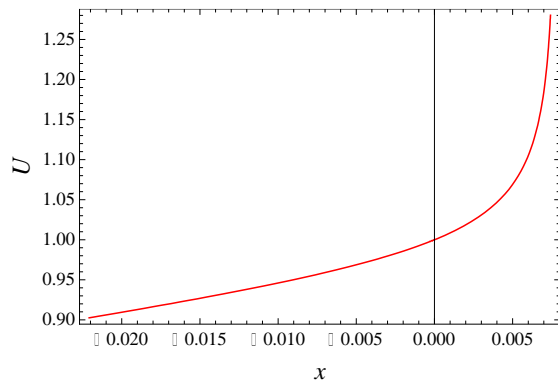


Figure 9: Variation of layer averaged velocity ($\beta=0.00028$, $C_D=0.005$, $\sigma=2$, $\gamma=0.5$)

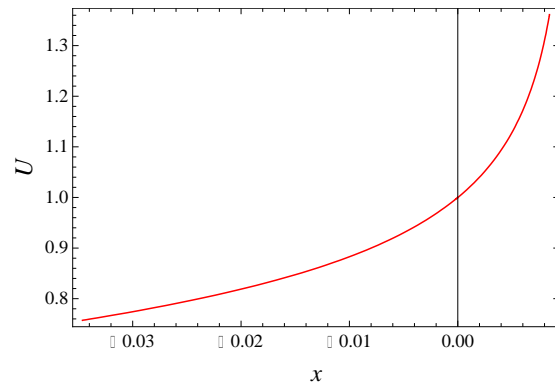


Figure 10: Variation of layer averaged velocity ($\beta=10$, $C_D=0.005$, $\sigma=2$, $\gamma=0.8$)

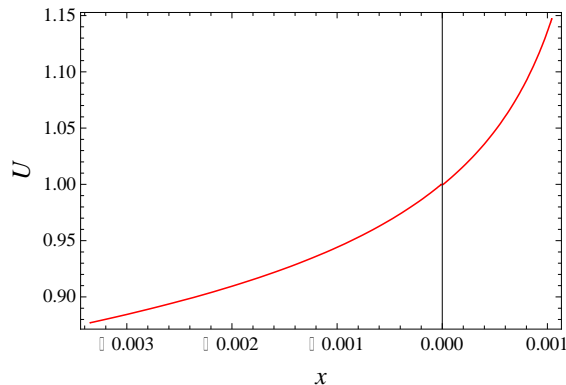


Figure 11: Variation of layer averaged velocity ($\beta=20$, $C_D=0.005$, $\sigma=2$, $\gamma=0.9$)

According to these figures β and γ do not significantly affect the layer averaged velocity. From equation 38, when the R , g , \tilde{C}_e , \tilde{v}_s and \tilde{Q} are constants, there is a linear relationship between the

suspendability and the drag coefficient. The minimum value that can be taken for drag coefficient is 0.002, and the maximum value is 0.02. The suspendability takes the value of 0.04 and 0.4 for the minimum and maximum values of the drag coefficient, respectively. Figures 12 and 13 show the variation of layer thickness and bed elevation according to the above conditions.

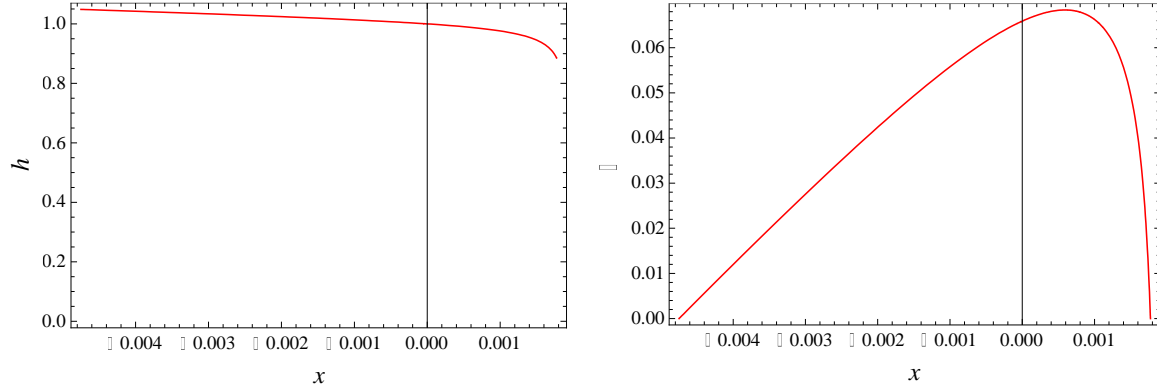


Figure 12: Variation of layer thickness and bed elevation ($\beta=0.04$, $C_D=0.002$, $\sigma=2$, $\gamma=0.5$)

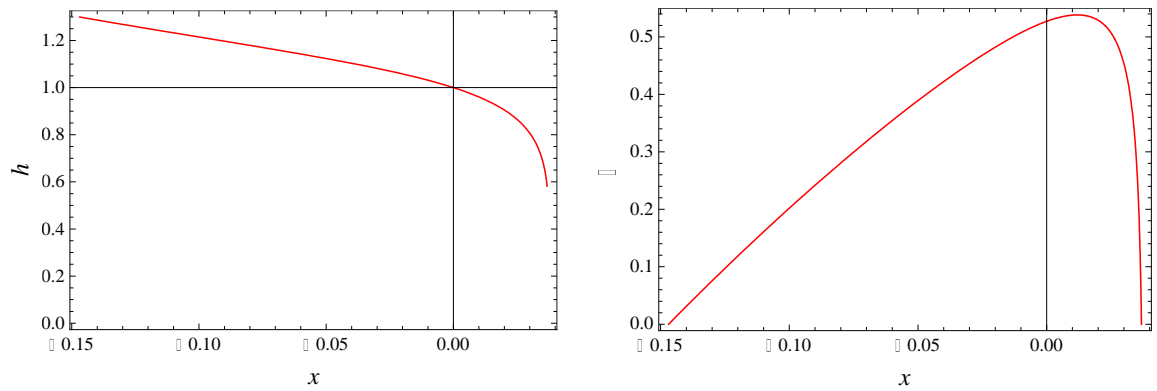


Figure 13: Variation of layer thickness and bed elevation ($\beta=0.4$, $C_D=0.02$, $\sigma=2$, $\gamma=0.5$)

According to Figures 3.10 and 3.11, the wavelength at $C_D=0.02$ is thirty times greater than at $C_D=0.002$. Also, the minimum layer thickness at $C_D=0.02$ is 1.4 times smaller than the value at $C_D=0.002$. When the drag coefficient is increasing, the bed elevation is also increased. It is clearly depicted in Figures 12 and 13. The slope of the continental shelf is generally as small as 0.001, when the value of the drag coefficient is equal to 0.01; when the value of the continental slope is around 0.025, the value of the drag coefficient is same as the above (Fildani *et al.* 2006). Figure 13. depicts the formation of a cyclic step in a continental slope. According to all these observations it was found that cyclic steps can be generated in shallow sea, continental slope, and deep sea.

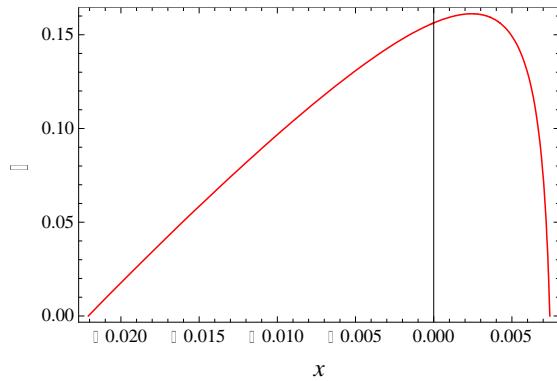


Figure 14: Variation of bed elevation without entrainment effect

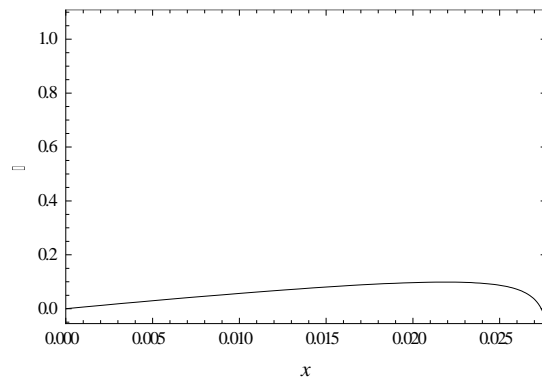


Figure 15: Variation of Bed elevation with the entrainment effect (Dias *et al.*2011)

Mathematical modeling of step shape bed forms generated by turbidity current incorporating the wave entrainment impact was done in previous research (Dias *et al.* 2011), where the variation of layer averaged velocity, the suspended sediment concentration, and the bed elevation with the flow direction were obtained. Figure 15 shows the variation of bed elevation observed by Dias *et al.*(2011). It was observed that the variation of layer averaged velocity and suspended sediment concentration are same in that previous research and the model develop in this analysis. However there are some differences in layer thickness and bed shape in the downstream end of the cyclic step. In the previous research there was a smooth bed formation in the downstream end, whereas in this model the generated step shape has an abrupt bed formation in the downstream end. However the shape of the cyclic step is approximately same in both studies.

CONCLUSION

In this research, an idealized mathematical model for the formation of cyclic steps without incorporating the wave entrainment impact was developed, and the shape of the cyclic steps which migrate upstream in a sub-aqueous setting, preserving their shape, was regenerated. The variation of layer averaged velocity, layer thickness, layer averaged suspended sediment concentration, and bed elevation over one wavelength, and the sensitivity of each governing parameter were also studied. According to the observations it was found that the cyclic steps can be generated in shallow sea, continental slope, and deep sea. The obtained results were acceptable and verified with the field observations and mathematical models developed by other researchers. When comparing this model with the previous research which was done with the entrainment effect, it was observed that entrainment does not significantly affect the formation of the cyclic step, but does affect its shape.

This idealized model is fundamentally important to understand the morphodynamic evolution of deep water depositional systems in a variety of tectonic settings and continental slopes, and deep sea re-construction work. Also, the model can be used to investigate the occurrence of cyclic step formation, which is important for construction work at sea. Further, the model can be used as secondary data, when studying sea flora and fauna.

REFERENCE

- Dias, D.D., Izumi, N., Yokokawa, M. (2011). Cyclic steps formed by turbidity currents. *Journal of Japan Society of Civil Engineers*, 503-510.
- Fildani, A., Normark, W.R., Kostic, S., Parker, G. (2006). Channel formation by flow stripping: Large scale scour features along the Monterey East Channel and their relation to sediment waves. *Sedimentology*, 1265-1287.
- Kostic, S., Parker, G. (2006). The response of turbidity currents to a canyon-fan transition: internal hydraulic jumps and depositional signatures. *Journal of Hydraulic Research*, 631-653.
- Kostic, S., Covault, J.A., Paull, C.K., Sylvester, Z., Fildani, A. (2016). Cyclic steps and related supercritical bedforms: Building blocks of deep-water depositional systems, western North America. *Marine Geology*, 4-20.
- Taki, K., Parker, G. (2005). Transportational cyclic steps created by flow over erodible bed. Part1. Experiments. *Journal of Hydraulic Research*, 488-501.

Sodium nickel phosphate cathodes used for sodium-ion rechargeable batteries

H.D.W.M.A.M.wijesinghe¹, V.P.S.Perera² and C. H. Manathunga^{1*}

¹*Department of Physics, Faculty of Applied Sciences, University of Sri Jayewardenepura, Nugegoda, Sri Lanka*

²*Department of physics, Faculty of natural sciences, Open University of Sri Lanka, Nawala, Nugegoda, Sri Lanka*

ABSTRACT

Although the traditional lithium-ion batteries have high capacities and performances, the price of those batteries increases rapidly. Sodium-ion batteries are predicted to be a suitable replacement for lithium-ion batteries in the future. In this case a suitable cathode for a sodium-ion battery was synthesized using a sodium nickel phosphate composite. The material was prepared using a solid state reaction of sodium phosphate and nickel (II) oxide. The synthesized material was characterized using a powder X-Ray diffraction method. The cathode was fabricated on aluminum foil using the synthesized material mixed with carbon black and polyvinylidene fluoride. Sodium metal pressed onto a copper plate was used as the cathode. After the fabrication of the cell, charge-discharge cycles and impedance measurements were performed to identify the electrochemical properties of the cell. The full discharge capacity of the cell was calculated to be 50.53 mA h g⁻¹. The high capacity of the cell indicates contribution from oxidation and reduction of cathode material other than the intercalation chemistry of lithium ions, which needs to be further investigated.

Keywords: *cyclic voltammetry; impedance; electrochemical measurements; potentiostat; three-electrode system*

INTRODUCTION

Considering the recent development of portable electronic devices, the demand for a high capacity battery was always highlighted. A number of rechargeable battery types were designed and developed, but the lithium ion battery (LIBs) is the most successful among them. Lithium ion batteries have shown high capacities over 300 mA h g⁻¹ (Zhang *et al.*, 2015), and is the common commercially available battery type. On the other hand lithium ion batteries are non-toxic and can be disposed easily (Zubi, Dufo-López, Carvalho & Pasaoglu, 2018) when compared with the previous battery technologies like mercury or lead. A number of cathode materials have been tested to use in lithium-ion batteries. Most of them consist of oxides and phosphates of active materials such as LiCoO₂, LiFePO₄ etc., while graphene is also considered as the most common type of anode material to produce the cell (Zhang *et al.*, 2015).

Among the drawbacks of the lithium ion battery technology, the most severe problem is that the limited abundance of lithium resources has led to the inflation of price (De Silva, Jayaweera, Perera, Jayarathna, & Rosa, 2014). It is predictable that the price may increase further because of the rapid depletion of available lithium resources, cost of the extraction and purification of Lithium and due to other contemporary issues as well. Therefore, soon or later a substitute for Lithium has to be found.

In such a quest sodium ion batteries may be a great option, as sodium resources are abundant and sodium can be extracted at a low cost.

Sodium ion batteries (SIBs) are considered to have similar electrochemical mechanism when compared with lithium ion batteries. This similarity has caused researchers to investigate them as an alternative to lithium ion batteries (Zhu *et al.*, 2018). Furthermore sodium ion batteries have a rocking chair mechanism similar to lithium ion batteries (Wang *et al.*, 2017). Sodium ion batteries would have a number of advantages if they can be used for high-power purposes. In general the charge transfer ability of sodium ions is considered to be faster than that of lithium ions due to weaker Lewis acidity and solvation of sodium ions (Kubota, Yokoh, Yabuuchi, & Komaba, 2014). According to some of the studies, sodium ion batteries are more suitable for large-scale energy storing systems in future because of their low cost, compared to lithium ion batteries at room temperature (Xie *et al.*, 2016).

Given the similarity between the electrochemical mechanisms of lithium ion and sodium ion batteries, scientists have tried a number of cathode materials which were successfully inserted in lithium ion batteries. These materials include sodium silicates (Law, Ramar, & Balaya, 2017), oxides, polyanions such as phosphates, pyrophosphates, fluoro sulfates, and oxychlorides, Na super ionic conductor types (NASICON), and organic compounds (Hwang, Myung, & Sun, 2017). However, all the materials which work well with lithium ion batteries do not show the same success with sodium ion batteries in general.

Nickel is a very popular cathode material in lithium ion batteries. Therefore, the possibility of using it as a cathode material for sodium ion batteries cannot be neglected. Lithium nickel oxide batteries have shown specific capacities around 275 mA h g⁻¹ (Nitta, Wu, Lee, & Yushin, 2015). This has caused nickel to be selected as a best choice to prepare rechargeable ion batteries. In addition to that nickel shows two main oxidation and reduction states (+II and +III). Hence the charge discharge mechanism not only depends on the intercalation chemistry but also on the oxidation and reduction process. This is the reason behind achieving relatively high capacities with nickel. However, using pure nickel oxide for the fabrication of LIBs does not work efficiently as supposed. This is because Ni²⁺ ions have the tendency to substitute Li⁺ sites during the synthesis and de-lithiation, which blocks the lithium diffusion pathways (Nitta, Wu, Lee, & Yushin, 2015).

Phosphate based cathode material design is relatively young and still needs to be developed. In contrast, MxPO₄²⁻ is a promising class of conversion cathode materials because of its thermodynamic stability (Zhao *et al.*, 2016). However, transition metal phosphates have been intensively investigated by researchers, because the strong P-O covalent bonds can stabilize the lattice oxygen even in a highly charged state. The phosphate framework materials show very low thermal expansion; this has led them to be having high structural stability at high temperature (Fang *et al.*, 2017). This paper is based on a cathode which was prepared to be accommodated in sodium ion batteries. To prepare the cathode, we used a sodium nickel phosphate composite. This composite was prepared using a simple solid state reaction of sodium phosphate and nickel oxide.

METHODOLOGY

For the preparation of the cathode material, nickel(II) oxide and sodium phosphate was used. Polyvinylidene fluoride (PVDF) and activated carbon was also used as the binder and charge transport material, respectively.

Preparation of Cathode Material

Cathode material was fabricated using a solid-state reaction. As the first step nickel (II) oxide and sodium phosphate was taken (the masses used correspond to equivalent molar ratios of NaNiPO_4) and ground using a universal ball mill at 600 r.p.m until a uniform fine-grained powder was formed. The powder was filtered to remove large particles and ground again using the same speed. The resulting powder was loaded into a crucible and was calcinated in the muffle furnace at 800 °C for three hours. The resultant was re-ground using a mortar and pestle. The powder thus formed was re-calcinated using the same temperature for another two hours.

Product Characterization

The product was characterized using powder X-Ray Diffraction (XRD) to identify phase and crystallinity of the synthesized material.

Battery fabrication and characterization

The synthesized material was used to fabricate cathodes of sodium ion rechargeable batteries as active material (AM). A 4 cm × 2 cm aluminum foil was used to prepare the cathode. A slurry was made by grinding the active material (0.8 g) with 0.1 g of activated carbon and 0.1 g of polyvinylidene fluoride (PVDF), dissolved in 1-methyl-2-pyrrolidinone, as the binder. The slurry was pasted using the doctor blade method on the aluminum foil such that a uniform thin layer was formed. The prepared cathode was dried using a hot plate at 100 °C. Battery fabrication was performed in an argon gas filled glove box. Metallic sodium pressed onto a copper plate was used as the anode. A cellulose membrane placed as the separator was soaked with the electrolyte consisting of a 1 M solution of NaClO_4 in propylene carbonate. The cell was covered with two glass plates, one on cathode side and the other on the anode side, and clipped well. The cell was loaded into an argon filled container where the electrodes were connected to the cell testing leads.

Electrochemical and impedance measurements

To determine charge discharge, the Potentiostat/Galvanostat HA-15 A, Science Workshop 750 Interface instrument, and Data Lab software were used. To take the impedance measurements, the GW Instek LCR-8101 instrument was employed.

Charging and discharging cycles were obtained at 0.5 mA current. Other than this a continuous series of charging and discharging was obtained galvanostatically using 0.4 mA current.

RESULTS AND DISCUSSION

The powder XRD pattern for the prepared material is shown in Figure 1. The peaks obtained from the range 20-30 degrees indicates that the material contains unreacted phosphate ions. The obtained XRD pattern was compared with the previous literature (Minakshi et al., 2016). It shows some characteristic peaks similar to previously known data. However there are some unknown peaks

also visible. This is due to the fact that a solid state reaction can contain impurities other than the desired product.

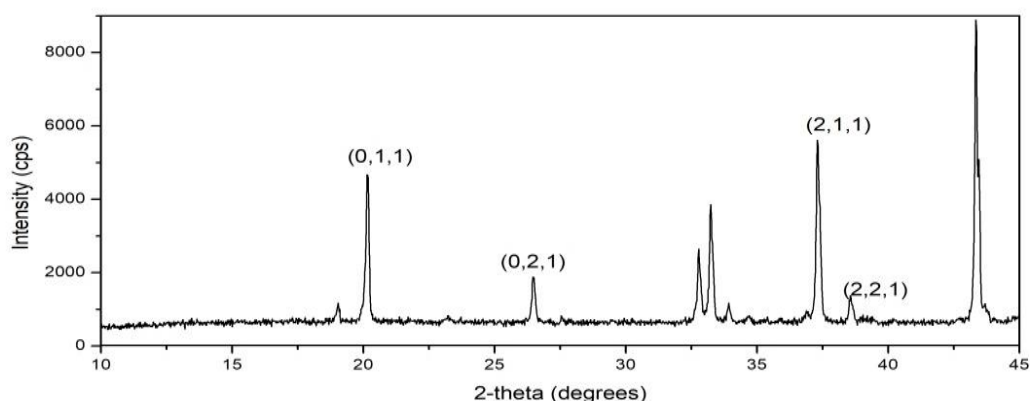


Figure 1: The XRD pattern for the prepared sample.

The battery charge cycle obtained using a 0.5 mA current is given in Figure 2. The charging curve shows an instant voltage increasing to a state around 2.2 V. With the time the curve stabilizes and achieves a steady state. Even if the charging time was extended further, the battery capacity was not changed dramatically.

After charging the cell in to a steady voltage around 2.2 V it was discharged at 0.5 mA, which is shown in Figure 3. The discharging curve shows a high discharging rate at the first few seconds and then the discharging rate decreases dramatically. The discharging curve shows that the cathode can hold charges for a reasonable time which may be due to oxidation and reduction phenomena other than the intercalation chemistry of the sodium ions. The full discharging capacity of the cathode was calculated using the following equation:

$$\text{Full discharge capacity (mA h g}^{-1}\text{)} = \frac{\text{Discharging current rate (mA)} \times \text{Time (in hours)}}{\text{Mass of the active material (in grams)}}$$

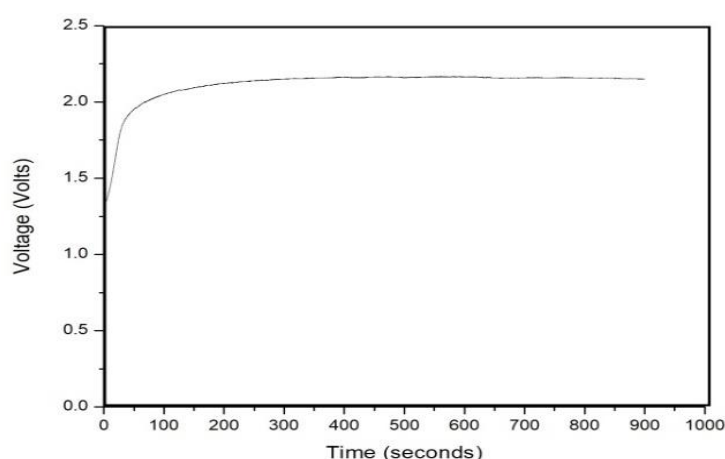


Figure 2. The charging curve

Figure 2: The charging curve for the cell

By substituting the relevant values to the above equation the discharging capacity was calculated to be $50.53 \text{ mA h g}^{-1}$.

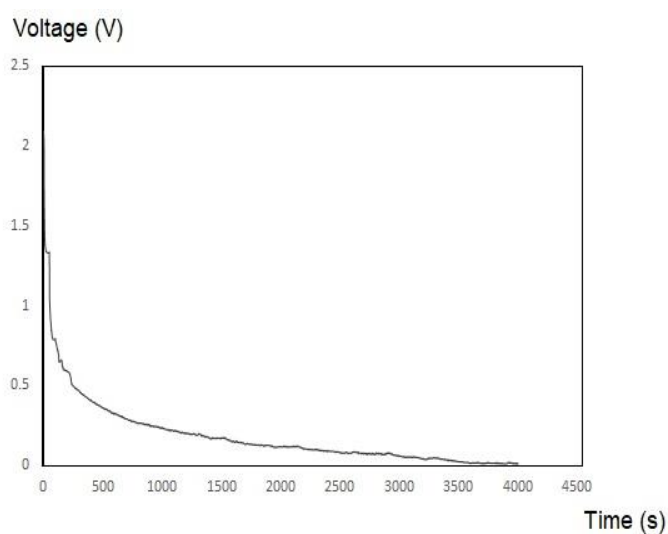


Figure 3. The discharging curve

The cyclibility of the cell was checked (Figure 4) by doing continuous charging and discharging cycles using 0.5 mA currents. Even after the 4500 seconds the discharging or charging pattern does not show a significant decrement.

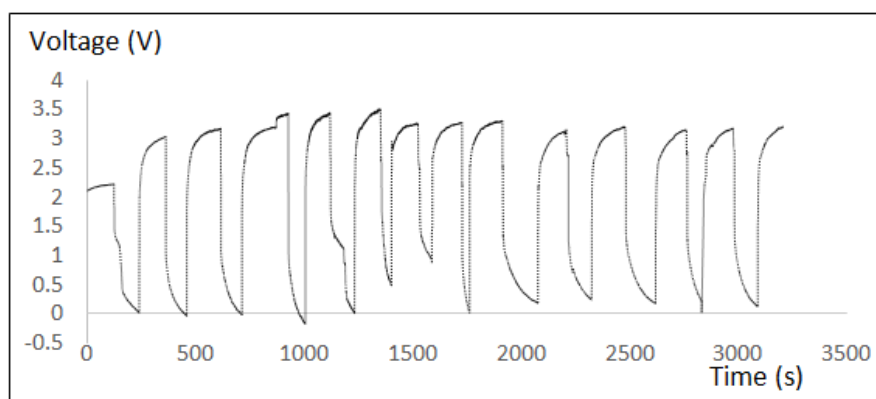


Figure 4: charging and discharging cycles using 0.5 mA currents

The obtained impedance curve for the cell is given in Figure 5. It shows that a large semi-circle is present in the lower frequency region and a small semicircle is present in the higher frequency regions. The smaller semicircle at the high frequency end represents the interface of the electrolyte with sodium anode. The large semi-circle in the lower frequency level shows the interface between electrolyte and the cathode.

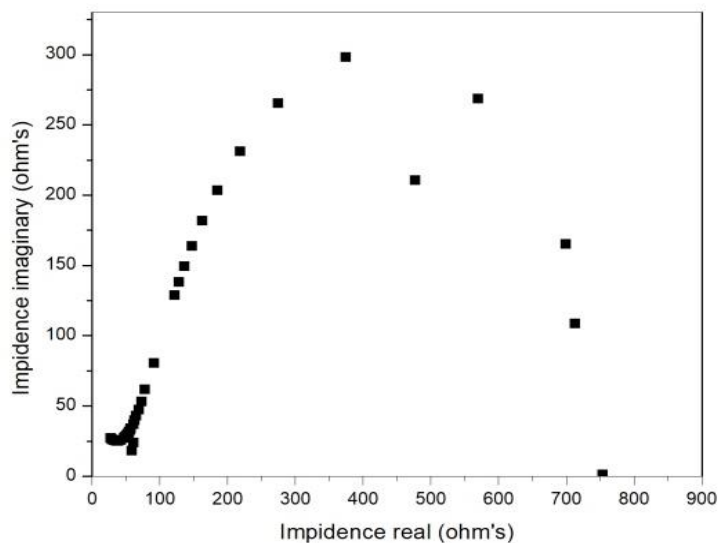


Figure 5: The obtained impedance curve the cell

CONCLUSION

The sodium nickel phosphate composite was successfully synthesized by using nickel(II) oxide and sodium phosphate. However due to the nature of the solid state reactions, unreacted materials were also visible in the prepared material. The full discharge capacity of the cell was $50.53 \text{ mA h g}^{-1}$.

ACKNOWLEDGEMENT

The authors would like to thank the Department of Physics, University of Sri Jayewardenepura for the funding under the grant No: ASP/01/RE/SCI/2016/24, and the Department of Physics, Open University of Sri Lanka, Nawala for the laboratory facilities. Further gratitude must be given to the Centre for Advanced Material Research, Faculty of Applied Sciences, University of Sri Jayewardenepura.

REFERENCE

- De Silva, R. C. L., Jayaweera, M. T. V. P., Perera, V. P. S., Jayarathna, I. P. L., & Rosa, S. R. D. (2014). Sodium nickel oxide nanoporous cathodes used for sodium-ion rechargeable batteries. *Sri Lankan Journal of Physics*, 15, 19-29.
- Fang, Y., Zhang, J., Xiao, L., Ai, X., Cao, Y., & Yang, H. (2017). Phosphate Framework Electrode Materials for Sodium Ion Batteries. *Adv Sci (Weinh)*, 4(5), 1600392.
- Hwang, J. Y., Myung, S. T., & Sun, Y. K. (2017). Sodium-ion batteries: present and future. *Chem Soc Rev*, 46(12), 3529-3614.
- Kubota, K., Yokoh, K., Yabuuchi, N., & Komaba, S. (2014). $\text{Na}_2\text{CoPO}_4\text{F}$ as a High-voltage Electrode Material for Na-ion Batteries. *Electrochemistry*, 82(10), 909-911.

Law, M., Ramar, V., & Balaya, P. (2017). $\text{Na}_2\text{MnSiO}_4$ as an attractive high capacity cathode material for sodium-ion battery. *Journal of Power Sources*, 359, 277-284.

Minakshi, M., Mitchell, D., Jones, R., Alenazey, F., Watcharatharapong, T., Chakraborty, S., & Ahuja, R. (2016). Synthesis, structural and electrochemical properties of sodium nickel phosphate for energy storage devices. *Nanoscale*, 8(21), 11291-11305.

Nitta, N., Wu, F., Lee, J. T., & Yushin, G. (2015). Li-ion battery materials: present and future. *Materials Today*, 18(5), 252-264.

Wang, D., Bie, X., Fu, Q., Dixon, D., Bramnik, N., Hu, Y.-S., . . . Du, F. (2017). Sodium vanadium titanium phosphate electrode for symmetric sodium-ion batteries with high power and long lifespan. *Nature Communications*, 1-7.

Xie, M., Huang, Y., Xu, M., Chen, R., Zhang, X., Li, L., & Wu, F. (2016). Sodium titanium hexacyanoferrate as an environmentally friendly and low-cost cathode material for sodium-ion batteries. *Journal of Power Sources*, 302, 7-12.

Zhang, Y., Li, Y., Xia, X., Wang, X., Gu, C., & Tu, J. (2015). High-energy cathode materials for Li-ion batteries: A review of recent developments. *Science China Technological Sciences*, 58(11), 1809-1828.

Zhao, W., Zhong, G., McDonald, M. J., Gong, Z., Liu, R., Bai, J., . . . Yang, Y. (2016). $\text{Cu}_3(\text{PO}_4)_2/\text{C}$ composite as a high-capacity cathode material for rechargeable Na-ion batteries. *Nano Energy*, 27, 420-429.

Zhu, Q., Cheng, H., Zhang, X., He, L., Hu, L., Yang, J., . . . Lu, Z. (2018). Improvement in electrochemical performance of $\text{Na}_3\text{V}_2(\text{PO}_4)_3/\text{C}$ cathode material for sodium-ion batteries by K-Ca co-doping. *Electrochimica Acta*, 281, 208-217.

Zubi, G., Dufo-López, R., Carvalho, M., & Pasaoglu, G. (2018). The lithium-ion battery: State of the art and future perspectives. *Renewable and Sustainable Energy Reviews*, 89, 292-308.

I. GENERAL INSTRUCTIONS

1) Research presented in the manuscript could be in any field of science. 2) The research work should not have been published or submitted for publication elsewhere. 3) A corresponding author who will be responsible for all communications with the SLAAS Office should be identified. 4) Submission of manuscripts: Manuscripts can be submitted by e-mail or regular mail to the Editor – SLAAS on or before 31st July, 2018. In case of submissions made through regular mail, The authors should forward three (03) hard copies of the manuscript and an electronic copy on a compact disc (CD) along with all other required documents. Authors are advised to mail the documents at least three (03) weeks prior to the deadline. 5) Certificate of authenticity: Declaration form attached hereto should be duly filled, signed by all authors and sent along with the manuscript. The authors who transfer the documents electronically should send the Certificate of Authenticity by regular mail. 6) Information of corresponding author: Duly filled form should be sent by regular mail. 7) Submissions that involve human or animal trials should provide evidence of approval obtained by an ethics review committee.

II. SPECIFIC INSTRUCTIONS TO AUTHORS

1. Document to be submitted ! Manuscript in MS Word (2003 or 2007 for Windows or later) format. ! A compact disk (CD) containing an electronic copy of the manuscript (for submissions by regular mail only). ! Duly filled and signed 'Certificate of Authenticity' form. ! Duly filled 'Information of Corresponding Author' form.

2. Format for typesetting

- Paper size: A4 (210 x 297) typed single sided only.
- Margins: Top, bottom and right margins of 25 mm and a left margin of 30 mm. 2
- Line spacing: 1.5 (18 points) throughout the text.
- Length: Length of the manuscript including text, tables, figures and references should not exceed 15 typed pages.
- Page and line numbering: All pages should be sequentially numbered using Arabic Numbers. All lines should also be numbered sequentially starting from the top to the bottom of each page.
- Font: Arial font, size 12. ! Language/spelling: UK English only.
- Software: Authors may use either MS Word 2003 or 2007/2011 for Windows or the Macintosh equivalent.

3. Title Page: Title page should include the following Information;

- Title and running title (less than 25 Characters). They should be in bold faced letters
- Name/s and affiliation/s of author/s
- Email address, mailing address and contact numbers of the corresponding author. Note: Identified the corresponding author by placing an asterisk after the name.

4. Abstract

Should be limited to a maximum of 250 words. Up to a maximum of the five (05) key word should be identified, arranged in alphabetical order, included immediately after the abstract. Abstract should be typed in italics. Scientific names in the abstract should be underlined.

No reference, tables, or figures should be included in the abstract.

5. Body

- Introduction: Justification of the research work, objectives and hypotheses should be included in the introduction.
- Methods and Materials/ Methodology: All materials, chemicals, clinical, subjects and samples used should be identified. Analytical, survey and statistical method should be explained concisely. Common analytical methods need not be elaborated.
- Results and Discussion: Can be combined.
- Conclusions: Should be concise.
- Headings: All headings should be in bold capital and centered, e.g., INTRODUCTION
- Subheadings: All subheadings should be in bold and in title case, e.g., Preparation of Land.
- Non-English terms: All non-English terms should be italicized, e.g., et al., i.e., viz., except "etc."
- References: Use APA style 3

6. Table and Figures

- Should be included in the exact place within the text
- Tables should be numbered sequentially using Arabic numerals. The titles should be self-explanatory and placed above the tables.
- Tables should not contain any vertical lines
- Illustration, Line drawing and photographs, if any, should be clear, properly numbered and captioned and ready for reproduction. They should be of high and resolution such as minimum of 300 dpi and saved in .tif or .bmp formats. Please do not use .jpeg or similar formats that do not reproduce well.
- All lettering, graph lines and points on graphs should be sufficiently large and bold faced to permit reproduction for inclusion in the Journal.
- Artworks and illustrations should be of appropriate thickness. Please note that thin lines do not reproduce well. Please note that the illustrations, line drawings and photographs should be placed in the appropriate location of the electronic file and numbered sequence with other figures.

7. Units

- SI units should be used.
- A single space should be left between the numerical value and the unit.

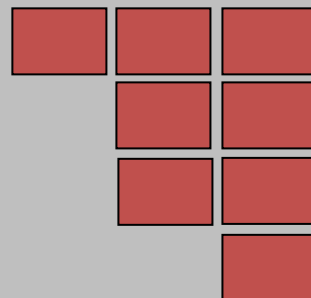
8. Acronyms and Abbreviations

- All acronyms should be written in full at the first time of appearance. Abbreviations can be used subsequently.
- The full stop should not be included in abbreviations. Where abbreviations are likely to cause ambiguity or may not be readily understood by readers, the units should be mentioned in full.

9. On being informed of the acceptance, the manuscripts should be revised as per the reviewers' suggestions and re-submitted to the Editor – SLAAS. The accepted manuscripts will be published in the inaugural Journal of the SLAAS. Manuscripts that do not confirm to the above guidelines will not be accepted.

10. Acknowledgements Only the essential individuals and/or organizations/institutes should be included

ISSN 1391-0256



*Journal of the Sri Lanka Association for
the Advancement of Science*

Volume 2 Issue 2

Contents

Research Articles

- 1. The impact of endoplasmic reticulum calcium concentration on transient cytosolic calcium response in phospholipase-C pathway: A simulation study**

J. T. H. Lakmal and S. P. Rajapaksha

- 2. Mathematical Modelling of Step Shape Bed Forms Generated by Turbidity Currents without incorporating the Wave Entrainment Impact**

H.M.K.N.Herath,* S.D.Sirithunge and D.D.Dias

- 3. Sodium nickel phosphate cathodes used for sodium-ion rechargeable batteries**



Edited and Published by the Sri Lanka Association of for the Advancement of Science

ISSN 1391-0256

